SANDIA REPORT
SAND2017-10469
Unlimited Release
Printed September 2017

Digital Rock Physics and 3D Printing for Fractured Porous Media

Mario J. Martinez, Hongkyu Yoon, Alec Kucala, Thomas Dewers, and Hector Mendoza

Prepared by
Sandia National Laboratories
Albuquerque, New Mexico 87185 and Livermore, California 94550

Sandia National Laboratories is a multimission laboratory managed and operated by National Technology and Engineering Solutions of Sandia, LLC, a wholly owned subsidiary of Honeywell International, Inc., for the U.S. Department of Energy's National Nuclear Security Administration under contract DE-NA0003525.

Sandia National Laboratories

Issued by Sandia National Laboratories, operated for the United States Department of Energy by National Technology and Engineering Solutions of Sandia, LLC.

Available to DOE and DOE contractors from
U.S. Department of Energy
Office of Scientific and Technical Information
P.O. Box 62
Oak Ridge, TN 37831

Telephone: (865) 576-8401
Facsimile: (865) 576-5728
E-Mail: reports@osti.gov
Online ordering: http://www.osti.gov/scitech

Available to the public from
U.S. Department of Commerce
National Technical Information Service
5301 Shawnee Rd
Alexandria, VA 22312

Telephone: (800) 553-6847
Facsimile: (703) 605-6900
E-Mail: orders@ntis.gov
Online order: http://www.ntis.gov/search

SAND2017-10469
Printed September 2017
Unlimited Release

Digital Rock Physics and 3D Printing for Fractured Porous Media

M.J. Martinez and A. Kucala
Fluid and Reactive Processes

H. Yoon and T. Dewers
Geomechanics

H. Mendoza
Structural & Thermal Analysis

Sandia National Laboratories
P. O. Box 5800
Albuquerque, New Mexico 87185-MS0836

Abstract

Imaging techniques for the analysis of porous structures have revolutionized our ability to quantitatively characterize geomaterials. Digital representations of rock from CT images and physics modeling based on these pore structures provide the opportunity to further advance our quantitative understanding of fluid flow, geomechanics, and geochemistry, and the emergence of coupled behaviors. Additive manufacturing, commonly known as 3D printing, has revolutionized production of custom parts with complex internal geometries. For the geosciences, recent advances in 3D printing technology may be co-opted to print reproducible porous structures derived from CT-imaging of actual rocks for experimental testing. The use of 3D printed microstructure allows us to surmount typical problems associated with sample-to-sample heterogeneity that plague rock physics testing and to test material response independent from pore-structure variability. Together, imaging, digital rocks and 3D printing potentially enables a new workflow for understanding coupled geophysical processes in a real, but well-defined setting circumventing typical issues associated with reproducibility, enabling full characterization and thus connection of physical phenomena to structure. Here we report on our research exploring the possibilities that these technologies can bring to geosciences for coupled multiscale experimental and numerical analysis using 3D printed fractured rock specimens.

ACKNOWLEDGMENTS

This work was supported by the Sandia National Laboratories Laboratory Directed Research and Development program, Project No. 191129. We appreciate discussions with David Noble (1516) concerning computational multiphase flows. We also thank Moo Lee (8864) for his advice and support with project management.

TABLE OF CONTENTS

FIGURES

EXECUTIVE SUMMARY

The main objective of this 2-year LDRD project was to explore the application of 3D printing (or more formally additive manufacturing) for geosciences. The idea was motivated by the recent confluence of high resolution imaging techniques for opaque materials, which has revolutionized our ability to characterize porous geomaterials, and mesoscale modeling using digital representations from these images. The diagram below summarizes the ultimate vision for digital rock physics coupled with 3D printing, suggesting the possibility to print replicas of porous structures for side-by-side testing and physics modeling. In the diagram, "validated constitutive models" are meant to represent new advanced constitutive laws which include defining characteristics of the pore structure.

The impact of such technology is to enable the creation of reproducible custom/functional porous specimens to test material response independent of pore structure variability – a potentially disruptive technology for geosciences. Moreover, it would enable the design of functional porous media with embedded sensors for energy and security applications.

Initially we explored whether we could in fact replicate pore structure at the scale of a sandstone, some of which can have sub-millimeter scale pores. Indeed digital copies of these micro- or nano-scale images can be printed, but not close enough to scale so as to not alter the governing physical processes that could be tested in the lab with printed specimens. Ultimately we decided to begin the research by investigating rock fractures, which were feasible to print and test at scale, and which are important for transport fluids and for geomechanics.

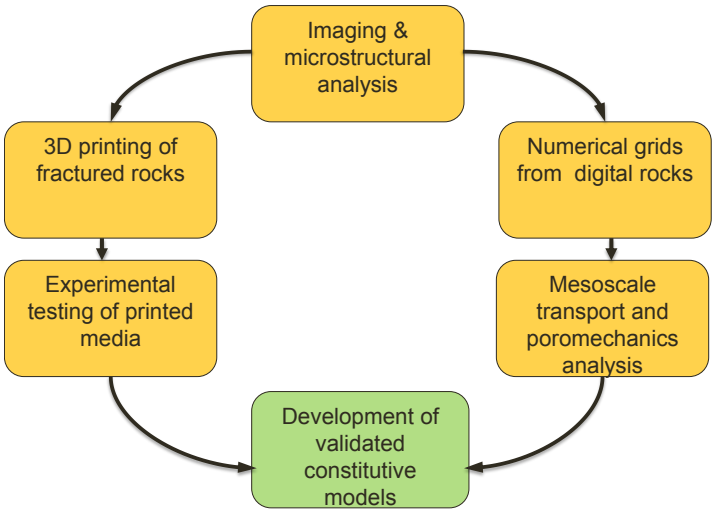

Digital rock physics and 3D printing workflow.

1. INTRODUCTION

Natural and many engineering geomaterials exhibit complex pore structures which greatly influence their mechanical, physical and chemical properties, including elastic moduli, strength, failure behavior, poroelastic parameters, seismic velocity, electrical conductivity, permeability, and wettability. These mechanical, physical and chemical properties of complex geo-materials are fundamental to accurately predicting multiphysical processes critical to emerging energy and climate issues. In geologic formations, coupling among thermal, mechanical, chemical and hydrological processes lead to complex behaviors across an enormous range of spatial and temporal scales. Subsurface strata are ubiquitously fractured at nearly every length of geotechnical interest; fractures control important subsurface phenomena such as seismicity, fast paths for fluid migration including, unconventional petroleum recovery, or leakage of carbon dioxide or hazardous waste materials from geologic storage. These coupled responses are also strongly influenced by the heterogeneity and induced anisotropy of microstructures.

Multiscale imaging techniques such as X-ray computed microtomography (micro-CT), laser scanning confocal microscopy, focused ion beam-scanning electron microscopy for the analysis of complex pore structures have revolutionized our ability to quantitatively characterize geomaterials. For example, three-dimensional digital representations of rock from micro-CT images and physics modeling based on these pore structures provide the opportunity to further advance our quantitative understanding of fluid flow, geomechanics, and geochemistry, and the emergence of coupled behaviors.

Additive manufacturing, commonly known as 3D printing, is a fast-growing manufacturing technique that produces custom parts or whole products by printing material by layers but only where it is needed. Compared to traditional manufacturing methods, 3D printing can alter products quickly for rapid prototype iteration or produce parts with multiple product designs. Some key benefits of additive manufacturing include short lead times, complex shapes, parts on demand, zero required inventory and less material waste. Even subtractive processing, such as milling and etching, may be economized by additive manufacturing. For the geosciences, recent advances in 3D printing technology may be co-opted to print reproducible porous structures derived from micro-CT of actual rocks for experimental testing. The use of 3D printed microstructure allows us to surmount typical problems associated with sample-to-sample heterogeneity that plague rock physics testing and to test material response independent from pore-structure variability. Together, imaging, digital rocks and 3D printing potentially enables a new workflow for understanding coupled geophysical processes in a real, but well-defined setting circumventing typical issues associated with reproducibility, enabling full characterization and thus connection of physical phenomena to structure.

In this project we utilized recent advances in 3D printing technology with a 3D digital rock approach to examine behavior of reproducible fractured porous structures derived from X-ray computed micro-tomography imaging of real fractured rocks. This project is a testbed to develop the methodology for use of additively manufactured copies of real rock in lab testing, which is a potentially disruptive technology for geosciences, engendering all manner of possible experiments on reproducible specimens.

2. PRINTING FRACTURED POROUS MEDIA

2.1. Workflow

3D printing of fractured and porous analog geomaterials has the potential to enhance hydrogeological and mechanical interpretations by generating engineered samples in testable configurations with reproducible microstructures and tunable surface and mechanical properties. For geoscience applications, 3D printing technology can be co-opted to print reproducible porous and fractured structures derived from CT-imaging of actual rocks and theoretical algorithms for experimental testing. In particular, the use of 3D printed samples allows us to overcome sample-to-sample variability that plagues rock physics testing, and to test material response independent from material variability. Recent advances in experimental methods and multi-scale imaging capabilities have revolutionized our ability to quantitatively characterize geomaterials and digital counterparts are now routinely used for numerical simulations to characterize petrophysical and mechanical properties across scales.

In this work we used a stereolithography (SLA) method to create a single fracture network. The fracture in shale was first scanned using a micro-CT system and then the digital fracture network was constructed. Aperture sizes in a single fracture network range from ~ 0.2 to ~1 mm. In particular, transparent fractured specimens based on 3D reconstruction of micro-fractured rock (i.e., 3D digital rock) were printed to study fluid flow characterization and manipulation. Here we describe the design of single fracture network and the progress of printing practices. CAD features have been integrated into the printing, including sample end pieces with a luer lock. With printed fracture samples, water inflow was tested to evaluate the impact of fracture aperture distribution on the 3D meniscus with the micro-CT system. Contact angle of water phase in 3D was analyzed. Various numerical simulations including (non-)reactive transport and multiphase flow cases are performed to study fluid flow characterization in a single fracture network.

2.2. Imaging and digital copies of a fracture network

X-ray computed microtomography (micro-CT, NorthStar) was used to scan a shale core sample and 3D-printed fracture network. Figure 2-1 shows the 3D view of micro-CT image of the shale core (1” diameter and 2” height) with proppants placed, a slice of micro-CT image, processed binary image, and reconstructed 3D fracture network. Briefly, the shale core was manually fractured parallel to the bedding direction, proppants (#20-30 clean sands) were distributed in a fracture to hold the fracture opening, and then the core with proppants was scanned with the micro-CT (Ingraham et al., 2015). A stack of images has been processed to distinguish the void space with solid (i.e., segmentation). A multiple set of filters (3D median, sharp contrast, contrast-limited adaptive histogram equalization, a few morphological operators) has been applied to enhance image segmentation as shown in Figure 2-1d. After segmentation, proppants were not considered for this work, instead a single fracture network was used to reconstruct a digital copy of the fracture (Figure 2-1e). A typical file format for 3D printing is the STL (stereolithography) file which was created using Simpleware ScanIP – 3D image segmentation and processing software. For our work, segmentation was performed using an in-house code and the binary file was processed to generate the STL file for 3D printing using Simpleware.

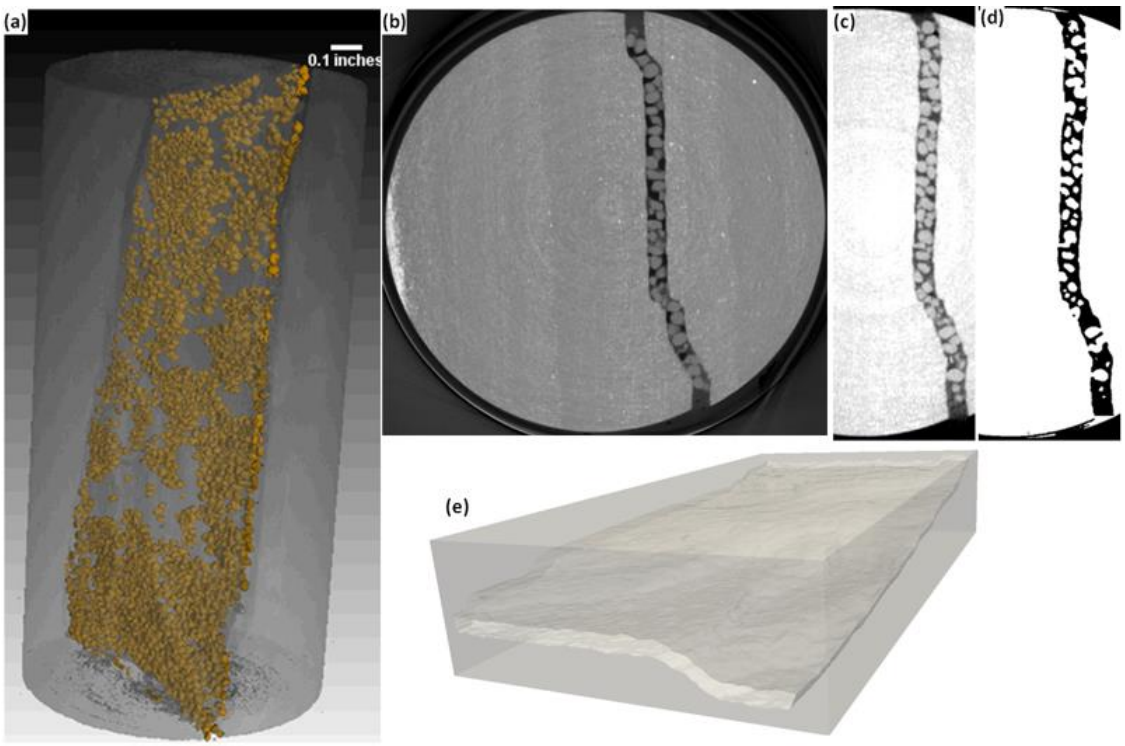

Figure 2-1. (a) 3D view of micro-CT image of a share core sample filled with proppants (in gold) in a single fracture network (from Ingraham et al., 2015). (b-c) MicroCT image slices. (d) Segmented binary image. (e) A single fracture network digitally reconstructed with segmented binary images.

2.3. 3D printers and materials for geoscience applications

Additive manufacturing, commonly known as 3D printing, is a fast-growing manufacturing technique that produces custom parts or whole products by printing material by layers only where it is needed. Currently, there are many popular and commercially available 3D printing techniques. Among these are fused deposition modeling (FDM), stereolithography (SLA), selective laser sintering (SLS), powder bed fusion (PDF), selective laser melting (SLM), electron beam melting (EBM) and polyjet are commonly used and widely adopted technologies (e.g., Gibson et al., 2015). For 3D printing materials, a variety of plastics (ABS, PLA), metals, photopolymers, light-curable resins, ceramics and composites can be used. Printing processes with different materials are also dependent on the type of printed products including the volume, feature size, strength, printing resolution, flexibility, or other functional purposes.

Single fracture network as shown in Figure 2-2(b) was printed using stereolithography (~20-30 μm printing layer) and granular-based printing (~100 μm resolution). First, the fracture was printed as one piece as shown in Figure 2-2(b&c) using several 3D printers including industrial production scale printers (e.g., 3D Systems ProJet MJP 2500, ProJet 6000 HD, ProJet CJP 460 Plus, Objet printers) and desktop scale printers (FormLabs Form1+ and 2). Two primary aspects of the printed fracture system were evaluated: (1) the connected fracture network at a real scale (i.e., printing feature resolution) and (2) how to clean materials left over inside the fracture network. We observed that most of printed samples did not produce the connected fracture network, but instead the network was not connected or only partially connected. To improve the connectivity and printing quality, fracture network printed with FormLabs printers was first

flushed with isopropyl alcohol (IPA) under ambient condition, followed by high air blow through the fracture network. One of the successful printed fracture and corresponding micro-CT image are shown in Figure 2-2(c&d). The design and printed fracture are also shown in Figure 2-2(f) and (g). In particular, the fracture itself can be printed at a finer scale (~ 30-50 μm), and can be used for molding or casting with other materials such as ceramics, cement, or clays.

To improve the printing quality of the fracture network and testability of the printed fracture network, the fracture network is split into the top and bottom parts as shown in Figure 2-3a. Since two parts are printed separately, it was much easier to design other features such as luer lock, inlet and outlet parts, and assembly units. Figure 2-3c shows the assembled fracture network with a water tight sealing material which is also 3D printed. This design improved the testing conditions of printed fracture network as well as printing quality of resolution.

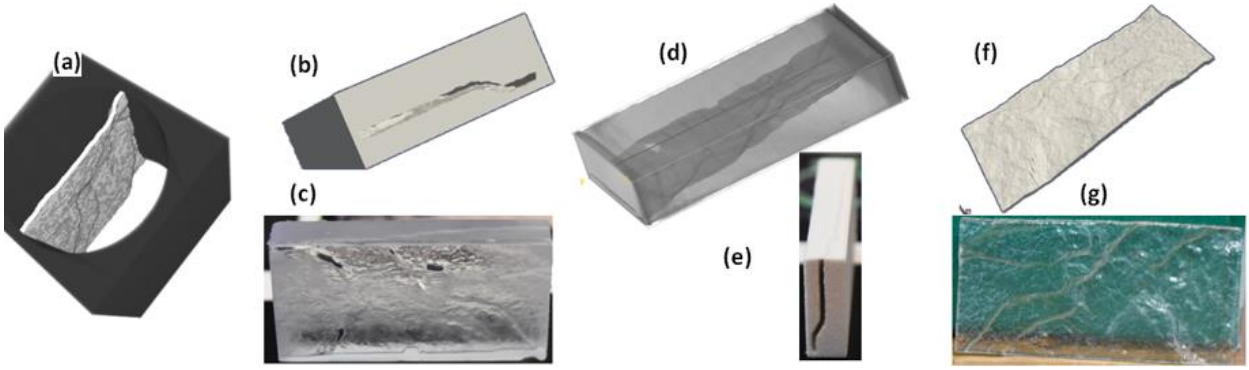

Figure 2-2. (a) Fracture network in a shale core as shown in Figure 2-1, (b) STL file of the fracture, (c) 3D printed fracture network of (b) using FormLabs Form1+, (d) microCT image of the printed fracture, (e) 3D printed fracture network of (b) using ProJet 460 with gypsum powders, (f) STL file of the fracture itself, and (g) the printed fracture.

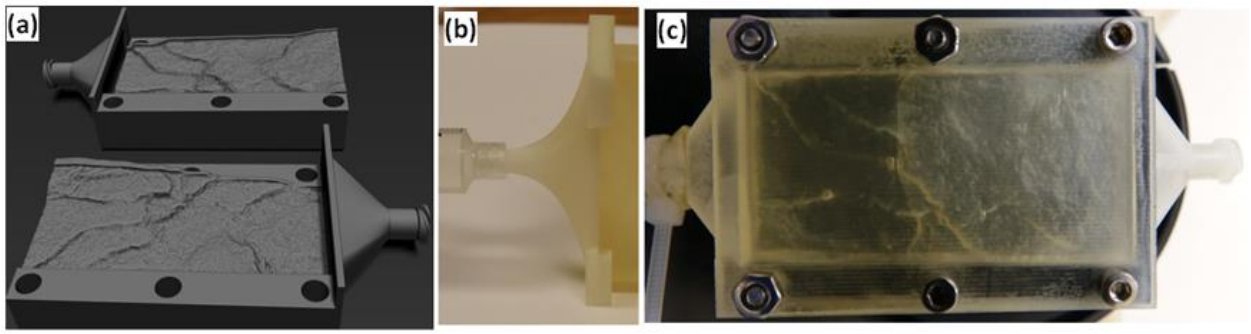

Figure 2-3 (a) Design of the fracture network with separate top and bottom parts, (b) a luer lock connection with a syringe, and (c) assembled fracture network with partially saturated water.

Another printing material suitable for geoscience applications is commercially available gypsum powder (calcium sulfate hemihydrates, $CaSO4 \bullet 0.5H_2O$, aka gypsum powder) (e.g., Bobby, 2014; Fereshtenejad and Song, 2016; Jiang et al., 2016; Ju et al., 2017). In particular, 3D Systems Projet 360/460 can be used with the powders by depositing a thin layer of powder onto

build chamber. A print head with binder jets dispenses a binder material where binding is required. The binding area is typically the design object. Finally, the build chamber is lowered and then repeated following the design. Typical dimension of the build bed is ~20-30 cm and the resolution of inkjet print heads is 300-500 dots per inch (~100 micron thick layer). Based on our experience, special features such as cracks or flaws can be printed at ~1mm feature resolution. In this work we used the ProJet 360/460 to create testing samples such as a typical cylindrical shape of rock testing samples as shown in Figure 2-4. Testing specimens are used to evaluate the effects of printing direction, the presence of flaws, and flaw geometry on the uniaxial compressive strength (UCS) and stress-strain behavior (Chapter 3).

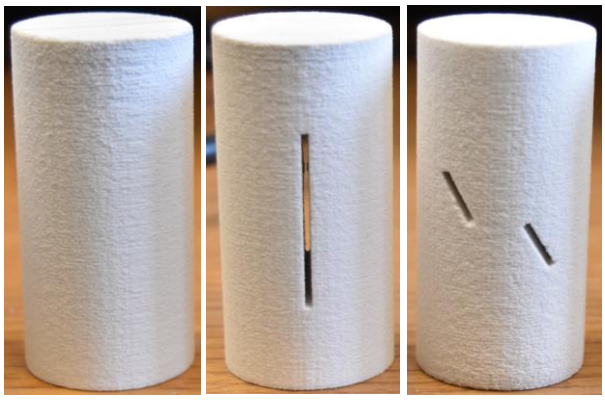

Figure 2-4. Core samples printed using gypsum powder (1" diameter and 2" height).

3. MECHANICAL PROPERTIES OF 3D PRINTED GYPSUM

3D printing of porous analog geomaterials has the potential to improve geomechanical understanding of rock behaviors by generating engineered samples in testable configurations with reproducible features and tunable mechanical properties. An example of powder-based 3D printed, a column is shown in Figure 2-4 and 3-1. First, 1" core sample was scanned with microCT before the UCS testing. MicroCT images (Figure 3-1(b&c)) show the anisotropy of directional printing and the non-uniform binder distribution, respectively. First, the UCS tests were performed on a 100 kN MTS load frame (Figure 3-1(d)) and later it was equipped with a 10 kN load cell to control the testing more precisely. Displacements were measured with a ±1.27 cm platen mounted extensometer. The specimens were compressed on the edge between a pair of the flat and parallel platens as seen in Figure 3-1(d). Tests were performed at a rate of 7.5×10^{-6} inch/sec for small cylindrical specimens. To measure the strain, the strain gauge was initially attached onto the powdered surface of the specimens as shown in Figure 3-1(f). The adhesive absorbed onto the surface of powdered sample so that it coupled the strain gauge onto the surface firmly. However, the outer shell of specimen around the gauge with the adhesive was separated from the main core, hence the displacements were not measured properly during the UCS testing. A preliminary data of stress-strain curve in Figure 3-1(e) also shows atypical volumetric strain curve due to this measurement error. A similar problem of the usage of adhesive was also reported in Fereshtenejad and Song (2016) where circumferential extensometer was alternatively used. Additional cause of the problem was the impact of the printing anisotropy on directional strain.

We also evaluated the impact of binder amount on the printed specimen. A default setting in ProJet 360/460 is the 100% binder usage. In general, 100% binder represents the efficient way to spread the binder to bond the gypsum powders. However, this setting uses the different amount of binder in the outer and inner areas, resulting in non-uniform distribution of the binder. In the powder-based 3D printing technique, powder particles and binder correspond to rock/soil grains and cement materials, respectively. Hence, the amount of binder is related to the degree of cementation in real geomaterials. For the horizontal direction and 0.1mm layer thickness, the UCS values of 100%, 150%, 180% of binder saturation levels were 5.48, 7.87, and 8.95 MPa, respectively.

Another aspect of the important behavior of geomaterials is dilatancy. For granular materials (e.g., soils), dilatancy can be attributed to the changes of grain packing, while for hard rocks, dilatany to microfracturing induced at the tips along the direction of the intragranular cracks (or defects) and/or along grain boundaries caused by the shear stress due to different stiffness in the grain distribution. Dilation due to microfracturing is in competition with compaction due to pore collapse (e.g., hardening). Figure 3-2 shows the volumetric strain behavior under UCS testing. A testing specimen was the horizontally printed gypsum sample (1.5" diameter, 3" height, 100% saturation level, 0.1mm layer thickness). A loading direction is in parallel to the printing direction. By a reference, the result of Mt. Simon sandstone is also shown (Figure 3-2d). Mt. Simon sandstone shows initial elastic behavior (see the initial unloading-loading cycles), yielding, and failure. As clearly demonstrated, total volumetric strain increases positively (i.e., compactional to the convention), followed by the change of direction to the negative

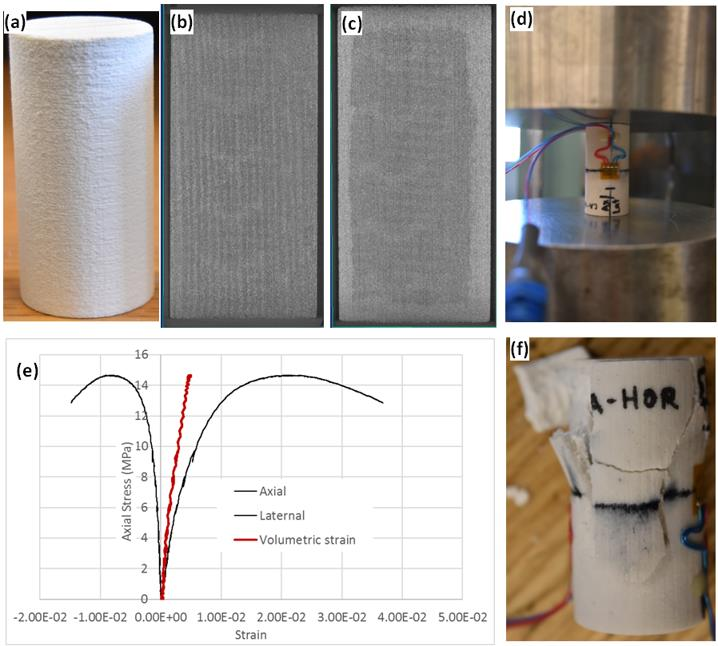

Figure 3-1. (a) 3D printed sample, (b-c) microCT image of the printed sample along the centerline without and with a post treatment of cyanoacrylate adhesive solution, (d) a photo of the UCS test, (e) stress-strain curve of the horizontally printed sample that was printed at 100% binder saturation level, and (f) sample photo taken after the UCS test reported in (e).

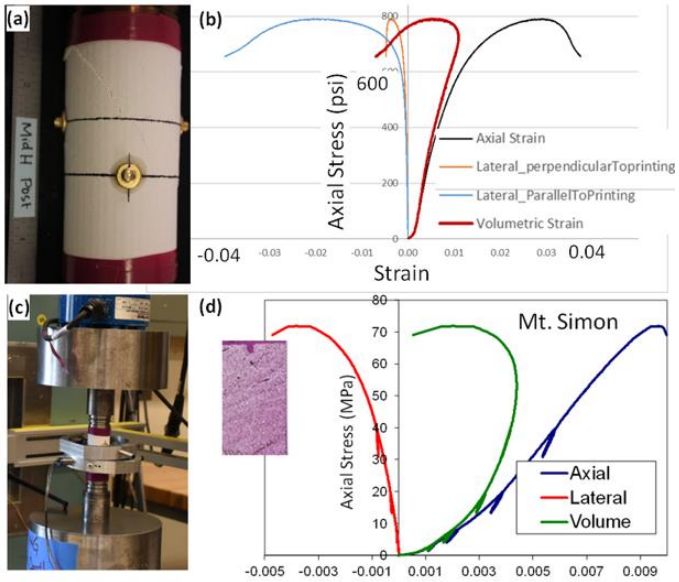

Figure 3-2. (a) Horizontal sample (1.5" diameter and 3" height) after the UCS testing. Buttons are for LDVT rings in (c). (b) Stress and strain curve of the horizontal sample. Four different strains are axial, two lateral (perpendicular and parallel to the printing direction), and computed volumetric strains. Two LVDTs were placed to measure the directional effect on the strain. (c) UCS testing setup. Note that the cylindrical load cell was used to minimize the loading effect on the end of sample. (d) Stress and strain curve of Mt. Simon sandstone sample reported in Dewers et al. (2014). A thin section of sandstone is inserted.

(dilatational). Based on the elastic strain calculated from the loading-unloading cycles, the elastic strain was computed, which led to a conclusion that the plastic volume strain is almost all dilatational rather than compaction. Similarly, the printed sample behaves initial elastic behavior, yielding, and failure. Unlike Mt. Simon sandstone, the stress-volumetric strain curve shows the quadrant of negative strain (Figure 3-2b), highlighting a highly dilatant behavior. For the printed sample this indicates that the volume of the specimen at the failure is greater than that of intact sample. It is also noted that the lateral strain is highly anisotropic depending on the printing direction and loading angle. As expected, the lateral strain parallel to the printing direction was much higher than that perpendicular to the printing.

To evaluate the impact of printing direction on the mechanical properties, at least three samples for each horizontal, 45°, and vertical direction were tested using UCS. Figure 3-3 shows the post failure pattern. In particular, the horizontally printed sample has a failure along the printing direction more significantly compared to other two directional samples. A few representative samples will be scanned with microCT to take a look at deformation and failure patterns. Failure surface will be also examined with profilometer to account for the surface roughness of the failure plane. For the UCS, horizontal, 45°, and vertical directional samples have 5.31, 2.67. and 4.49 MPa, respectively. Overall these results indicate that the strength of the printed samples and geomechanical behavior of the samples can be highly dependent upon the printing direction. Directional strength and strain behaviors will be also accounted for by velocity (P- & S-waves) measurements.

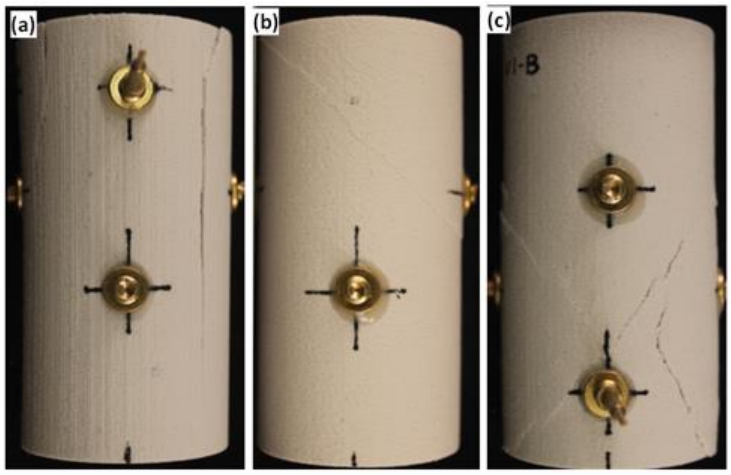

Figure 3-3. Post-testing samples printed (a) horizontally, (b) at 45°, and (c) vertically. The loading was applied vertically.

4. SINGLE-PHASE FLOW AND TRANSPORT IN A REAL FRACTURE

This chapter discusses our research with reactive flow and transport in a real fracture, depicted in Figure 4-1. The fracture surface is rough and dips with respect the enclosing rock body. Moreover, the fracture is not planar.

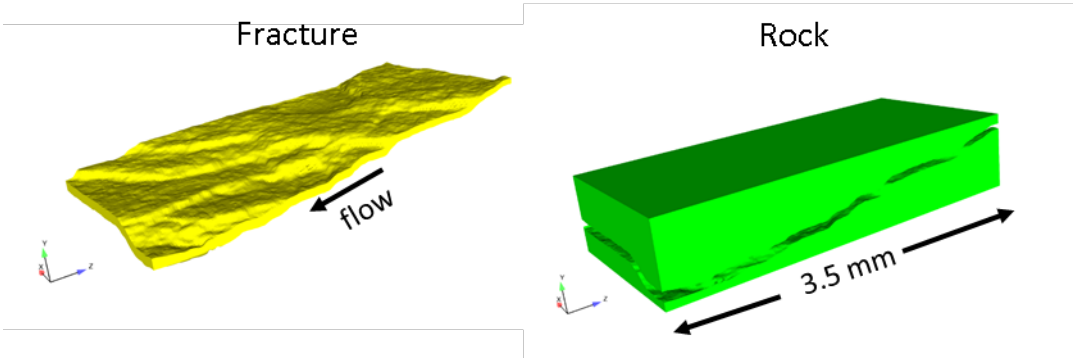

Figure 4-1. Digital rock fracture. Original fracture is shown in Figure 2-1.

4.1. Grids for digital rock physics

Voxel representations of CT scans can be used directly in fluid and solid mechanics simulation software. The resulting representations of interfaces between phases (e.g. solid vs void) are of course "stair-stepped." Unstructured-grid FEM based software in the SNL Sierra package, used in some of the analyses discussed below, can provide a better representation of CT scanned images and of evolving phase interfaces (e.g. multiphase flows).

For example, in the present case of the embedded fracture in Figure 4.1, an StereoLithography (STL) file of the fracture surfaces is generated from the segmented CT scan. A uniform grid of tetrahedral elements is generated for the entire block including the embedded fracture. The CDFEM Level Set method (Chapter 5) in Sierra/Aria is used to cut this block grid with the STL representation of the fracture surfaces. The CDFEM also provides local grid refinement on the level sets representing the fracture surfaces, resulting in separate unstructured grid blocks for the fracture and the surrounding solid ("rock"), separated by interfaces with the same level of fidelity that was in the original STL file. Different physics can be solved in the fracture and rock domains, and general interface boundary conditions can be applied on the fracture surfaces.

4.2. Permeability

The permeability of 3D printed fracture network was experimentally measured using constant head permeability test. Due to the highly conductive fracture network, the head difference was maintained at 0.3-1 cm. An average measured permeability was 0.19 mm^2 which was much higher than that estimated from numerical simulations described below (see Table 4-1). To account for this difference, we analyzed the aperture size distribution from micro-CT images of the printed fracture assembly as shown in Figure 4-2. As described earlier and seen in Figure 4-2(b), a gasket of 1 mm thickness was used to prevent water leaking. As a result, the aperture distribution ranged from ~1.2mm to ~2.2 mm. As listed in Table 4-1, the difference of average aperture is ~ 1mm which is identical to the thickness of the gasket. Although the presence of the

gasket caused the assembled fracture to be wider, the workflow developed to design the fracture network is very promising due to the fact that the difference is only attributed to the gasket. In addition, micro-CT imaging is a very powerful technique to evaluate the integrity of the assembled fracture network. We are currently redesigning to hold the gasket so that the aperture will reflect the real sample more accurately.

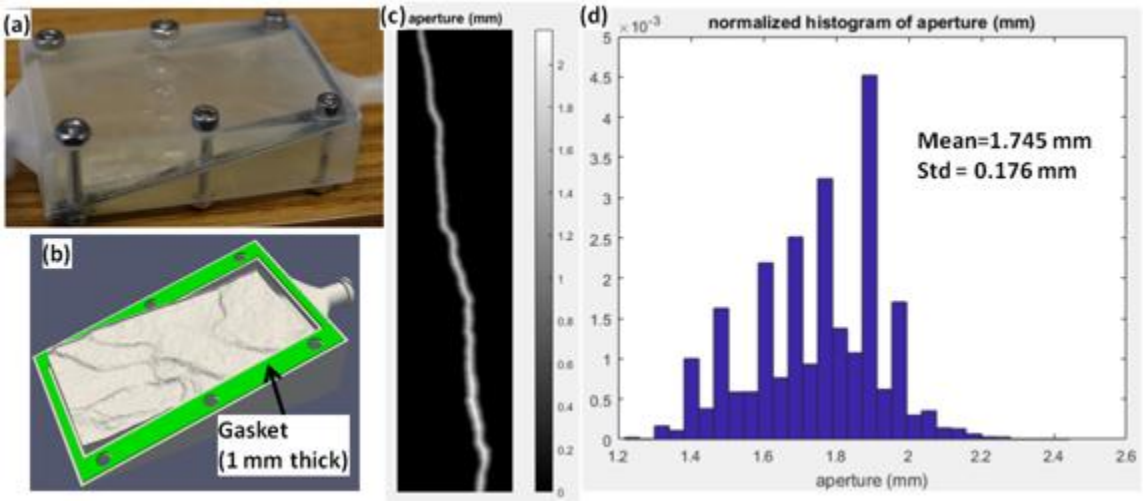

Figure 4-2. (a) Assembled fracture network. Note that the steel screw was replaced with nylon for microCT imaging. (b) STL format of the bottom part of the fracture with a gasket of 1mm thickness. (c) Aperture distribution calculated from the segmented microCT image. (d) Normalized histogram of aperture distribution over a stack of microCT images (540 images).

The permeability was computed by simulating Navier-Stokes fluid flow directly in the digital fracture. A uniform inflow was applied on the upstream edge of the fracture and a constant pressure on the downstream end. The upper and lower fracture surfaces are no-slip surfaces. The side surfaces (orthogonal to the flow direction) are slip surfaces. Various levels of grid refinement were used to show grid convergence. The area-averaged pressure over the inflow area was used in the discrete Darcy's Law, $v = (k/\mu)\Delta p / L$, where L is the length of the rock block along the flow direction in Figure 4-1, to determine the implied permeability. The permeability thus determined is given in Table 4-1. It is worthwhile noting that this permeability is determined from the complete 3D fluid dynamics equations solved in a non-planar, rough fracture.

A common approximation to modeling fluid flow in fractures is by applying the lubrication approximation, often referred to as the cubic law approximation [Brown, 1987]. The lubrication approximation, as applied in the present context, amounts to assuming the local fracture roughness is gradual (small slope) and hence the volume flow can be approximated by the lubrication equation. The lubrication equations can be derived as the depth-averaged continuity equation for flow in a variable aperture fracture,

$$\nabla \bullet \mathbf{Q} + \frac{\partial(\rho b)}{\partial t} = 0 \qquad (1)$$

where $b = b(x, y)$ is the local fracture aperture. The average mass flux assumes the lubrication (small slope roughness) approximation,

$$\mathbf{Q} = \rho b \mathbf{v} = -\frac{\rho b^3}{12\mu}\nabla p\,, \tag{2}$$

so that for a two-dimensional fracture lying in the x-y plane the mass balance equation takes the form,

$$\frac{\partial}{\partial x}\left(\frac{\rho b^3}{12\mu}\frac{\partial p}{\partial x}\right)+\frac{\partial}{\partial y}\left(\frac{\rho b^3}{12\mu}\frac{\partial p}{\partial y}\right)=\frac{\partial(\rho b)}{\partial t} \tag{3}$$

Since the subject fracture is not planar, as assumed in the foregoing development, the local aperture was computed in the local (average) normal direction, resulting in the permeability (perm = $b^2/12$) map in Figure 4-3. The flow is modeled on the two-dimensional domain by applying a specified uniform flow rate on an inflow boundary and uniform pressure on the outflow boundary. The effective permeability for the fracture is then computed using the area-averaged pressure difference across the fracture using the Darcy Law shown above. Table 4-1 shows reasonable agreement between the cubic law and the fluid dynamics models, with about a 20% difference in effective permeability between the two simulation techniques. In the table the hydraulic aperture is based on the computed permeability.

Table 4-1. Effective Fracture Properties

Method	Permeability (mm^2)	Hyd. Aperture (mm)
Navier-Stokes	0.0405	0.697
Cubic Law	0.034	0.639
Experimental	0.19	1.745

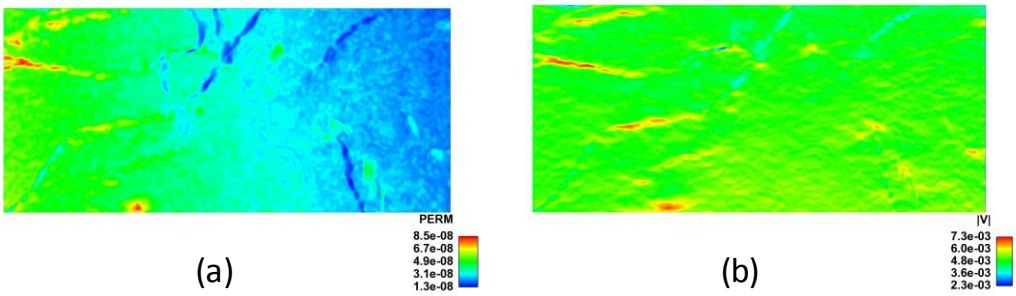

Figure 4-3. Cubic law approximation of (a) fracture permeability, and (b) steady Darcy flow (m/s).

4.3. Dispersion of a passive tracer

The dispersion of a passive scalar in a natural fracture is an important characteristic which determines the distribution and fate of solutes in fractured media [Grisak & Pickens, 1980; Keller et al., 1999; Detwiler et al., 2000].

The dispersion is calculated in the fracture depicted in Figure 4-1 using the steady 3D Navier-Stokes flow solution discussed above. The transport of a passive scalar is modeled by the advection-diffusion equation,

$$\frac{\partial C}{\partial t} + \nabla \bullet \left(\mathbf{v}C - \mathbf{D} \bullet \nabla C \right) = 0 \qquad (4)$$

Where C is the concentration, $\boldsymbol{v}$ is the 3D Navier-Stokes velocity field and D is the molecular diffusion coefficient.

The no-slip boundary condition on the fracture surfaces induces large gradients in the concentration field and can amplify numerical perturbations. In order to eliminate under-resolved concentration waves (wiggles), say from and imposed a Dirichlet value for concentration at the inflow boundary, a smooth initial concentration is imposed.

A smooth initial concentration condition was imposed to minimize high frequency spatial disturbances in the subsequent numerical transport. The initial concentration was specified as

$$C_0 = \frac{M}{4\pi t\sqrt{D_{xx}D_{yy}}} \exp\left(-\frac{\phi}{4t}\left(\frac{\left(x - x_0 - Ut/\phi\right)^2}{D_{xx}} + \frac{\left(y - y_0\right)^2}{D_{yy}} \right) \right) \qquad (5)$$

This formula is the solution to a convected pulse of strength M at elapsed time t. For use as an initial condition, the strength M and (fixed) time, t, are chosen to set $\max(C_0)$ of unity, with support in about half the fracture width.

The dispersion was calculated for various values of Peclet number, Ub/D , where U is injected flow velocity, 0.005 m/s, and b is the average hydraulic aperture, 0.7 mm. We considered diffusion coefficients in the range 10^{-6} – 10^{-9} m^2/s, corresponding to Peclet numbers 3.5 – 3500.

As a point of reference to estimate the necessary discretization in space and time required for a given quality of solution, we solved the 2D analytical solution given in the previous equation. We used the same uniform flow rate and diffusion coefficients on the 2D domain, as depicted in Figure 4-3, using sufficiently resolved mesh spacings to reproduce the analytical solution. The break-through profiles at the outflow boundary are shown in Fig 4-4(a). These profiles are virtually exact compared with the analytical values. The lowest diffusion coefficient results in nearly pure advection of the initial profile, while the highest coefficient results in significant attenuation.

For the 3D transport simulation, we used the mesh sizes found in the 2D test simulation to give accurate results. Figure 4-4(b) shows the mean concentration (averaged over the outflow area) at the outflow plane for a wide range of diffusion coefficients. The solutions for low diffusion coefficients especially show non-Fickian behavior, and long tails. Inspection of the solutions indicates the long tail for Pe = 3500 ($D=10^{-9}$ m^2/s) corresponds to "trapping" of contaminant in the surface roughness where the no-slip condition prevents efficient convective transport.

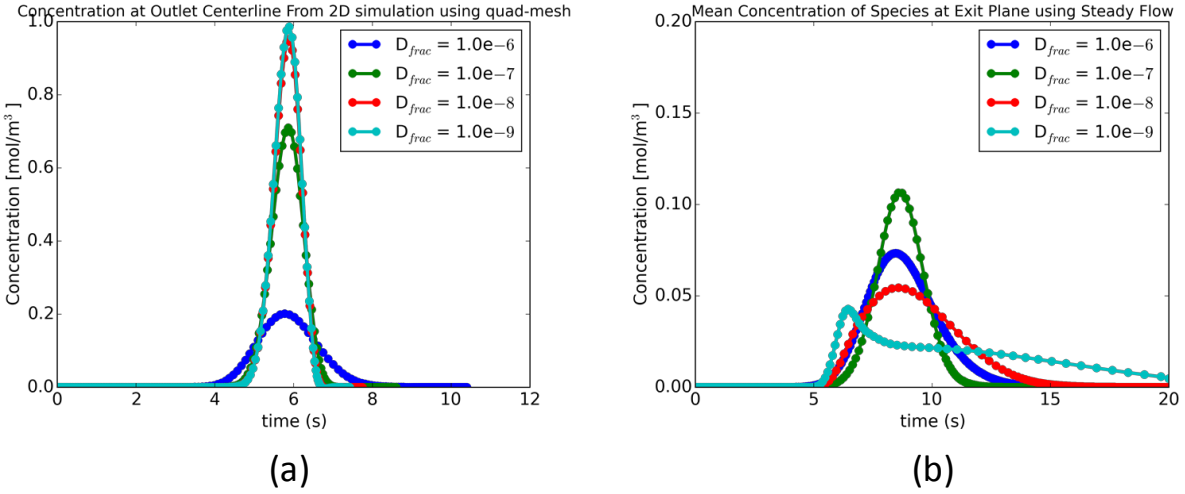

Figure 4-4. (a) Break-through concentration for 2D transport, (b) mean outflow concentration in 3D transport with Navier-Stokes flow. Diffusion coefficients are in m/sec; corresponding Peclet numbers, based on the mean aperture (0.7 mm), range between 3.5 ($D=10^{-6}$) to 3500 ($D=10^{-9}$).

Given the complexity of the flow field and concentration patterns, the dispersion was calculated by the method of moments (e.g., Dagan, 1989). The zero moment (which is simply the constant mass in the domain before breakthrough) is,

$$M = \int_{\Omega} c(\mathbf{x},t)d\Omega \tag{6}$$

where Ω denotes the whole volume of the 3D fracture. The first moment maps the center of mass trajectory $(x_i = (x,y,z), \bar{X}_i = (\bar{X},\bar{Y},\bar{Z})$,

$$\bar{X}_i = \frac{1}{M}\int_{\Omega} x_i c(\mathbf{x},t)d\Omega \tag{7}$$

And the second central moments,

$$\bar{X}_{t,i} = \frac{1}{M}\int_{\Omega}\left(x_i - \bar{X}_i\right)^2 c(\mathbf{x},t)d\Omega, \qquad i = 1,2,3\ , \tag{8}$$

provide information on the dispersion characteristics. The local dispersion is

$$D_{tot,i} = \frac{1}{2}\frac{d}{dt}\bar{X}_{t,i} \tag{9}$$

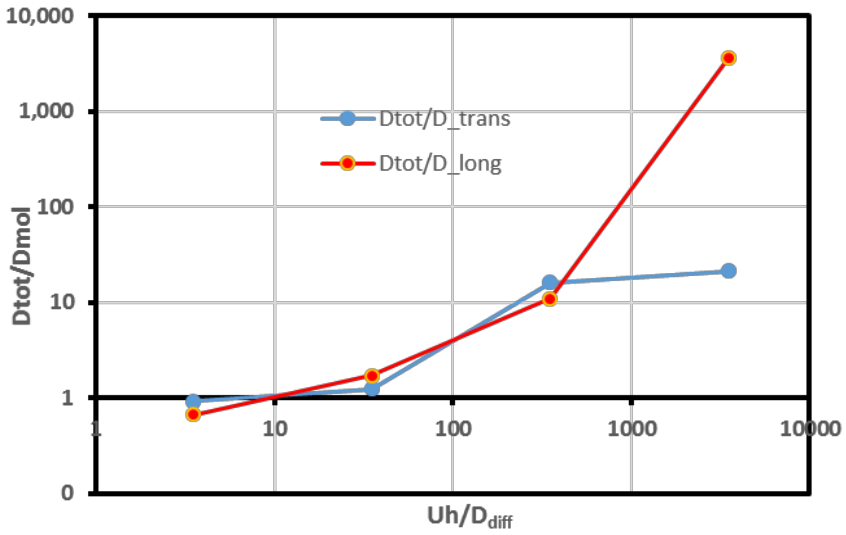

Figure 4-5. Dispersion in the 3D fracture computed by method of moments. The red curve denotes the ratio of longitudinal (streamwise) dispersion to the molecular diffusion coefficient. The blue curve denotes the ratio of transverse (cross-stream) dispersion to molecular diffusion coefficient.

The subscript denotes "total" dispersion because it includes the molecular diffusion component. The mean values of longitudinal and transverse dispersion thus computed are shown in Figure 4-5, where the ordinate denotes the ratio of the total dispersion to the molecular diffusion. At Pe = 350 the total dispersion is about 10 times the molecular diffusion, both along and orthogonal to the main flow direction, while at Pe = 3500 the total longitudinal dispersion exceed 3000 times the molecular diffusion.

4.4. Fracture closure by thermal expansion

We numerically investigated the closure of the rock fracture due to thermal expansion. To approximate *in-situ* conditions of a deeply buried subsurface fracture, the exterior boundaries of the rock block were confined against normal displacement. Upon introduction of hot water flow in the fracture, the rock heats up by thermal diffusion (assuming the rock is impermeable to flow) and undergoes thermal expansion and closure of the fracture. Figure 4-6(a) shows a snapshot of the rock and fluid temperature at 93 seconds and Figure 4-6(b) shows the vertical stress component and the velocity magnitude in the fracture at 360 seconds. Figure 4-7 shows the time history of the fracture flow area at the inflow boundary and the reduction in water volume flux under a fixed pressure difference across the fracture. Hot water injection in deeply buried fractured rock may induce fracture close and reduce permeability. The flow area and volume flux decrease by about 10% over the time span shown.

Injection of cold water in the fracture would induce rock contraction and fracture opening. If the main compressibility of the bulk rock is due to the fractures, this suggests a permeability increase due to fracture opening in geothermal or engineered geothermal systems where in-situ heat is extracted by circulating cool water through a fracture network.

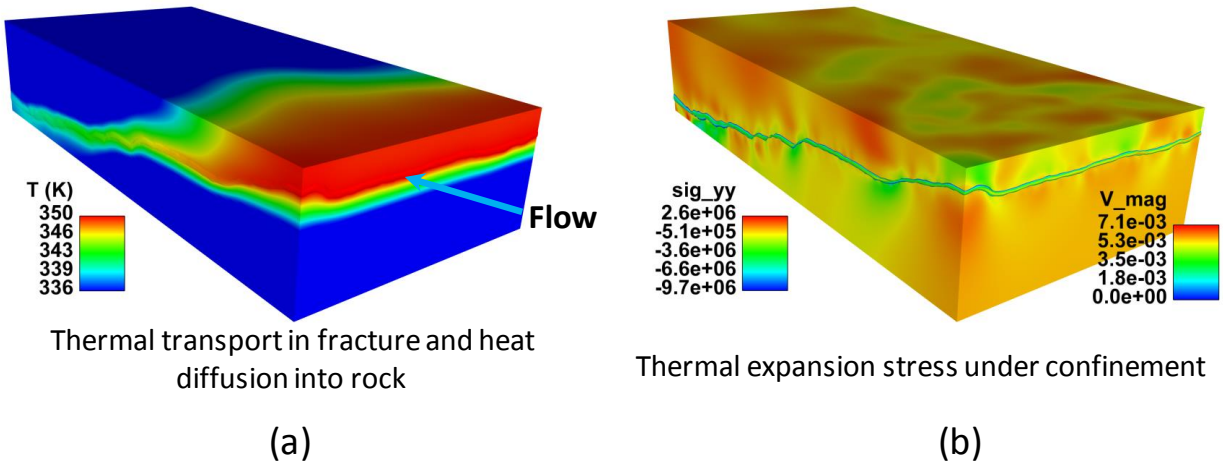

Figure 4-6. Thermal closure of a rock fracture.

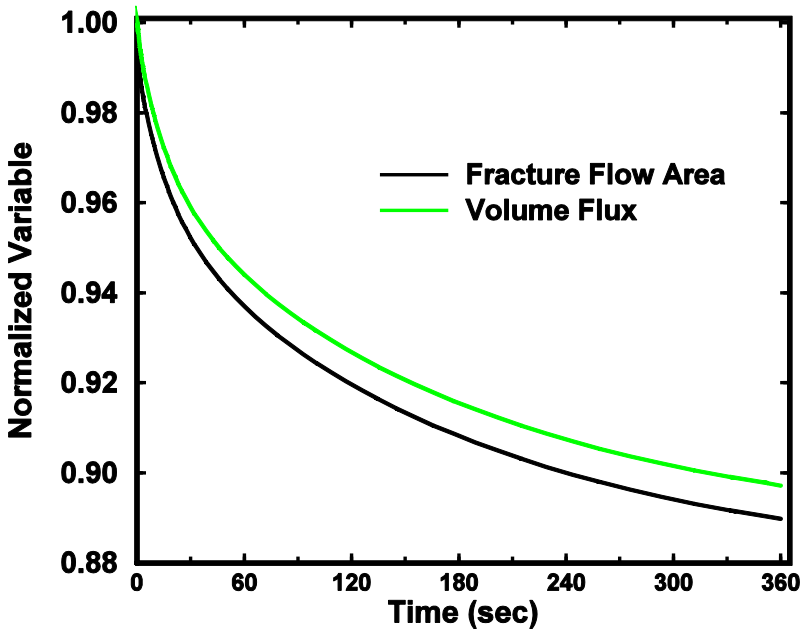

Figure 4-7. Fracture inflow area reduction with rock expansion and corresponding flow rate reduction under fixed pressure gradient.

5. A NEW WETTING MODEL FOR FINITE ELEMENT METHODS

An enriched finite element method is described for capillary hydrodynamics including dynamic wetting (Noble *et al*., 2017). The method is enriched via the Conformal Decomposition Finite Element Method (CDFEM). Two formulations are described, one with first-order accuracy and one with second-order accuracy in time. Both formulations utilize a semi-implicit form for the surface tension that is shown to effectively circumvent the explicit capillary time step limit. Sharp interface boundary conditions are developed for capturing the dynamic contact angle as the fluid interface moves along the wall. By virtue of the CDFEM, the contact line is free to move without risk of mesh tangling, but is sharply captured. Multiple problems are used to demonstrate the effectiveness of this method.

5.1. Methodology

5.1.1. Conformal Decomposition Finite Element Method

In (CDFEM), the finite element space is enriched by decomposing the finite elements that span the zero level set into subelements that conform to the original element and the zero level set surface. In this work, the computational domain is assumed to be discretized by piecewise triangular elements in two dimensions (2D) or tetrahedral elements in three dimensions (3D). Thus, the interface consists of line segments in 2D, and triangles in 3D. The result of the decomposition is a fully connected finite element mesh of triangles or tetrahedrons that conform to the instantaneous locations of the materials and their interfaces. The conformal decomposition process is much like element refinement for non-conformal adaptivity. The elements are subdivided into new elements and nodes are added in the process, and field data at newly added nodes are populated, or prolonged, using existing field data. Unlike nonconformal adaptivity, however, the new elements conform to the material domains, and the added nodes lie on the interfaces between the materials, as illustrated in figure 5-1.

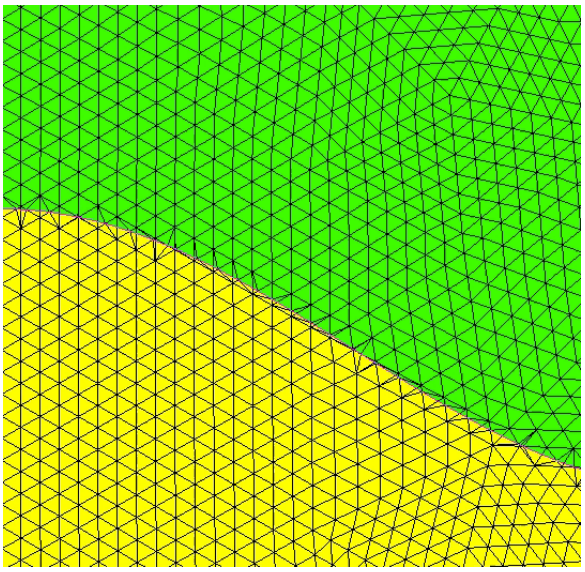

Figure 5-1. An example of conformal mapping where an interface separates two phases in the flow (yellow and green blocks), adding degrees of freedom directly to the background mesh.

5.1.2. Second order capillary stabilization

Second-order temporal accuracy can be obtained by the following proposed algorithm:

1. Navier-Stokes predictor: Solve the Navier-Stokes equation using semi-implicit term with old interface location for the predicted velocity, $\tilde{\boldsymbol{u}}$ (equations 9 and 10)
2. Solve level set equation using predicted velocity (equation 11)
3. Perform conformal decomposition, creating the domain Ω^{n+1}
4. Navier-Stokes corrector: Solve the Navier-Stokes equation using the moving mesh term and semi-implicit term, now based on the velocity correction (equations 12 and 13)

$$\int_{\Omega^{\mathrm{n}}} \rho\left(\frac{\frac{3}{2}\tilde{\boldsymbol{u}} - 2\boldsymbol{u}^{\mathrm{n}} + \frac{1}{2}\boldsymbol{u}^{\mathrm{n-1}}}{\Delta t} + (\tilde{\boldsymbol{u}}\cdot\boldsymbol{\nabla})\tilde{\boldsymbol{u}}\right)\cdot \boldsymbol{w}_{\mathrm{i}}\mathrm{d}\Omega + \int_{\Omega^{n}} -P\mathbf{I} + \mu(\boldsymbol{\nabla}\tilde{\boldsymbol{u}} + \boldsymbol{\nabla}\tilde{\boldsymbol{u}}^{t})\cdot\boldsymbol{\nabla}\boldsymbol{w}_{\mathrm{i}}\mathrm{d}\Omega + \int_{\Gamma_{\mathrm{f}}^{\mathrm{n}}} \sigma\left((\mathbf{I}-\mathbf{nn}) + \Delta t\underline{\boldsymbol{\nabla}}\tilde{\boldsymbol{u}}\right)\cdot\boldsymbol{\nabla}\boldsymbol{w}_{\mathrm{i}}\mathrm{d}\Gamma = 0, \tag{9}$$

$$\int_{\Omega^{\mathrm{n}}} (\boldsymbol{\nabla}\cdot\tilde{\boldsymbol{u}})\boldsymbol{w}_{\mathrm{i}}\mathrm{d}\Omega = 0, \tag{10}$$

$$\int_{\Omega^{\mathrm{n}}} \rho\left(\frac{\frac{3}{2}\phi^{\mathrm{n+1}} - 2\phi^{\mathrm{n}} + \frac{1}{2}\phi^{\mathrm{n-1}}}{\Delta t} + \tilde{\boldsymbol{u}}\cdot\boldsymbol{\nabla}\phi^{\mathrm{n+1}}\right)\boldsymbol{w}_{\mathrm{i}}\mathrm{d}\Omega = 0, \tag{11}$$

$$\int_{\Omega^{\mathrm{n+1}}} \rho\left(\frac{\frac{3}{2}\boldsymbol{u}^{\mathrm{n+1}} - 2\boldsymbol{u}^{\mathrm{n}} + \frac{1}{2}\boldsymbol{u}^{\mathrm{n-1}}}{\Delta t} + \left((\boldsymbol{u}^{\mathrm{n+1}} - \dot{\boldsymbol{x}})\cdot\boldsymbol{\nabla}\right)\boldsymbol{u}^{\mathrm{n+1}}\right)\cdot\boldsymbol{w}_{\mathrm{i}}\mathrm{d}\Omega + \int_{\Omega^{\mathrm{n+1}}} -P\mathbf{I} + \mu(\boldsymbol{\nabla}\boldsymbol{u} + \boldsymbol{\nabla}\boldsymbol{u}^{\mathrm{t}})^{\mathrm{n+1}}\cdot\boldsymbol{\nabla}\boldsymbol{w}_{\mathrm{i}}\mathrm{d}\Omega + \int_{\Gamma_{\mathrm{f}}^{\mathrm{n+1}}} \sigma\left((\mathbf{I}-\mathbf{nn}) + \Delta t\underline{\boldsymbol{\nabla}}(\boldsymbol{u}^{\mathrm{n+1}} - \tilde{\boldsymbol{u}})\right)\cdot\boldsymbol{\nabla}\boldsymbol{w}_{\mathrm{i}}\mathrm{d}\Gamma = 0, \tag{12}$$

$$\int_{\Omega^{n+1}} (\nabla \cdot \boldsymbol{u}^{n+1}) \boldsymbol{w}_i \mathrm{d}\Omega = 0 \qquad (13)$$

Here, the semi-implicit term in the momentum predictor (Δt term in the third line of equation 12) is used to incorporate the effect of the moving interface, since the integration conforms to the old interface location. After updating the level set field ϕ using the predicted velocity $\tilde{\boldsymbol{u}}$ (equation 11), the conformal decomposition is performed, which enables the solution to capture the weak discontinuity in the velocity and strong discontinuity in the pressure. In order to get an updated solution on the now updated mesh Ω^{n+1}, the momentum equation is solved again to obtain $\boldsymbol{u}^{n+1}$ (equations 12 and 13). To obtain second-order temporal accuracy, the BDF2 time integrator is used for both the level set and momentum equations.

The notable differences between the predictor (equations 9 and 10) and corrector (equations 12 and 13) are the domains of integration, the moving mesh term in the corrector, and the fact that the semi-implicit term in the corrector is based on the velocity correction instead of the full velocity field. For all Navier-Stokes solves, PSPG and SUPG stabilization are employed. These terms are not shown here, however, for clarity.

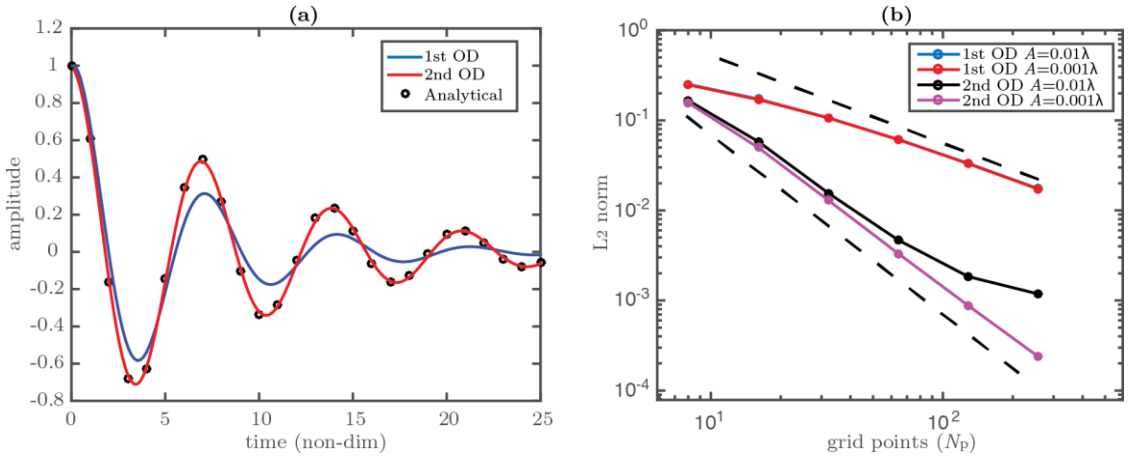

Figure 5-2. Model comparisons with analytic results of Prosperetti (Prosperetti, 1981) for 1st and 2nd order simulations; (a) Sinusoidal temporal wave decay of fluid interface amplitude, (b) Convergence of $\boldsymbol{L_2}$ norm as a function of grid points $\boldsymbol{N_p}$ on a fixed computational domain for 1st and 2nd order simulations at different initial disturbance amplitudes. Dashed lines represent expected 1st and 2nd order convergence.

The damped oscillation of two immiscible viscous fluids with finite surface tension σ is simulated within the presented finite-element framework and compared with the analytical solution provided by Prosperetti (Prosperetti, 1981). Here, a small amplitude sinusoidal disturbance of wavelength $\lambda = 2\pi$ is superimposed on two fluids each occupying half of the two-dimensional computational domain and separated by a common interface with surface tension σ. Second order accuracy in time can be observed in figure 2(a), where the analytical solution of Prosperetti shows favorable agreement with the present results, especially when compared to a first-order treatment of the problem at the same time stepping interval. Obviously, much lower time steps are required for the first-order method. In both cases, the

effect of the capillary stabilization allows for a stable solution, although the second order method allows for more accurate solutions. Second order convergence is also observed in figure 2(b) in the L_2 norms of the interface heights h.

5.1.3. Sharp interface conditions for dynamic wetting

CDFEM allows for the boundary conditions to be applied in a sharp manner along the wetting line where the fluid interface meets the domain boundary. Two types of boundary conditions are combined to provide accurate wetting behavior. First, a sharp version of the Navier slip condition is applied all along the wall to capture behavior that transitions from wetting line motion to no-slip like behavior away from the wetting line. Second, a traction boundary condition pulling at the equilibrium contact angle captures the fine scale effect of wetting that cannot be captured well with reasonable mesh sizes.

The Navier-Slip boundary condition imposes a traction on the fluid proportional to the difference between the fluid velocity and the wall velocity. This boundary condition is attractive in dynamic wetting applications where the no-slip condition must be relaxed to allow the wetting line to move along the wall (Dussan, 1979; Cox, 1986). Using consistent finite element integration, the contribution to the momentum equation for the Navier-slip condition is given as

$$\int_{\Gamma_w^{n+1}} \frac{\mu}{\beta^*} (\boldsymbol{u}_w - \boldsymbol{u}^{n+1}) \cdot \boldsymbol{w}_i \mathrm{d}\Gamma \tag{14}$$

where Γ_w is used to denote wall boundary of the fluid, $\boldsymbol{u}_w$ is the wall velocity, and β^* is the slip length describing the strength of the resistance to flow along the wall. This must be determined from experiments and is dependent on the wetting properties of the fluids and the mesh size. Due to the sharp nature of the velocity on the contact-line, integration of equation (14) is carried out in a nodally lumped fashion whereby the contributions are integrated on the node points as opposed to the Gauss points. This is done to remove spurious oscillations in the vicinity of the contact line.

The Laplace-Beltrami form for surface tension incorporates an edge term where the fluid interface meets the external boundary. As described in Ganesan, 2014 this term can be used to weakly specify the equilibrium contact angle. This accomplished by assembling an additional term in the momentum equation by integrating along the contact line,

$$\int_{\zeta^{n+1}} \sigma(\cos(\theta_s)\boldsymbol{t}_w + \sin(\theta_s)\,\boldsymbol{n}_w) \cdot \boldsymbol{w}_i \mathrm{d}\Gamma \tag{15}$$

where ζ is the contact line, θ_s is the static contact angle, and $\boldsymbol{t}_w$ is the tangent to the wall oriented in the direction of fluid interface normal and $\boldsymbol{n}_w$ is the wall normal. This term only weakly imposes the equilibrium contact angle which allows the dynamic contact angle to develop as a natural balance of the forces at the wall. The only free parameter in this system of boundary conditions is the dimensionless slip coeffcient β^*. Just as is done for the slip condition, this traction is specified as a vector condition, rather than limiting it to the tangent direction. The normal direction is zeroed using a Dirichlet condition on the velocity component normal to the wall to enforce the no penetration condition.

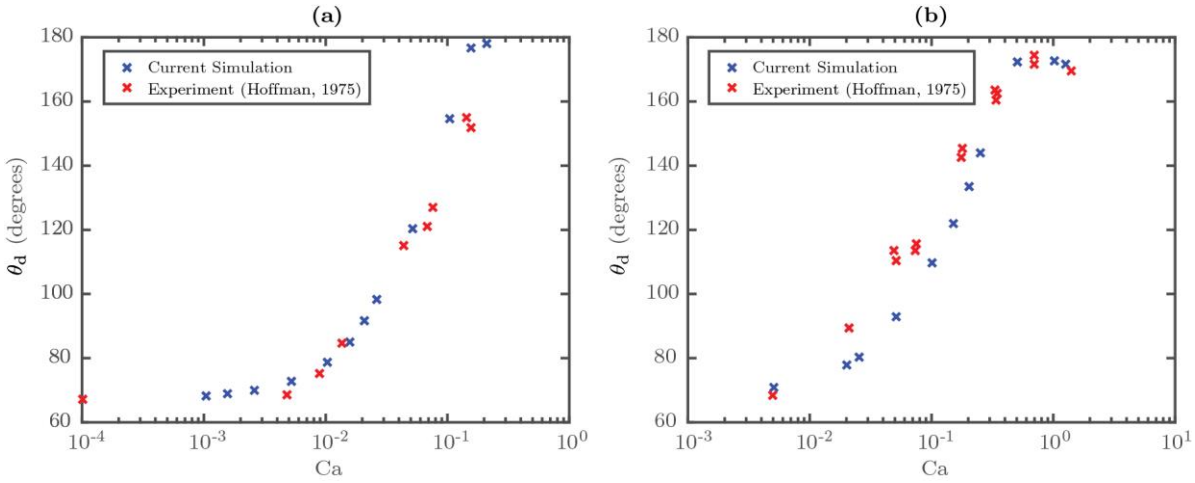

Figure 5-3. Model comparisons with dynamic angle experiments of Hoffman, 1975 at various capillary numbers; (a) Santicizer 405, (b) Ashland Chem. Admex 760. The slip length $\boldsymbol{\beta^* = 4.0 \times 10^{-8}}$ m is held constant between both fluids.

Here we demonstrate the ability of our wetting model to accurately replicate the experiments of Hoffman, 1975 which show the dynamic contact angle θ_d dependency on local capillary number $\mathrm{Ca} = \mu U_i/\sigma$ where U_i is the injection velocity at the bottom of the tube. Comparisons between our simulations and the experiments of Hoffman for two fluids, Santicizer 405 and Admex 760 immersed in air are made. To fit the experimental data, the real slip length β^* was adjusted until good agreement with a single data point was found. The simulations were then ran with this fixed slip length across a large range of capillary numbers and compared with experiment. The agreement with the experiment is excellent, shown in Figure 5-3 where $\beta^* = 4.0 \times 10^{-8}$ m. This demonstrates the ability of our wetting model to intrinsically model the capillary number dependence on dynamic angle at the contact line with fitting only a single parameter β^*, irrespective of fluid type.

Next, we focus on accurately capturing the dynamics of a liquid rising in a vertical capillary tube, where the intrinsic wetting properties of the fluid forces the meniscus to rise until the inertial, viscous, gravitational, and surface tension forces become balanced. Due to the complex interaction between these forces, our model must be fit to and compared with experimental data. In this pursuit, we use the experimental air-water circular-tube capillary rise data provided in Heshmati & Piri, 2014 as a means to validate our wetting model. In this air-water experiment, the radius of the capillary tube $r = 0.65$ mm, the working fluid is water. For all cases, the density and viscosity for air are prescribed as 1.17 kg/m^3 and 1×10^{-5} Pa s, respectively.

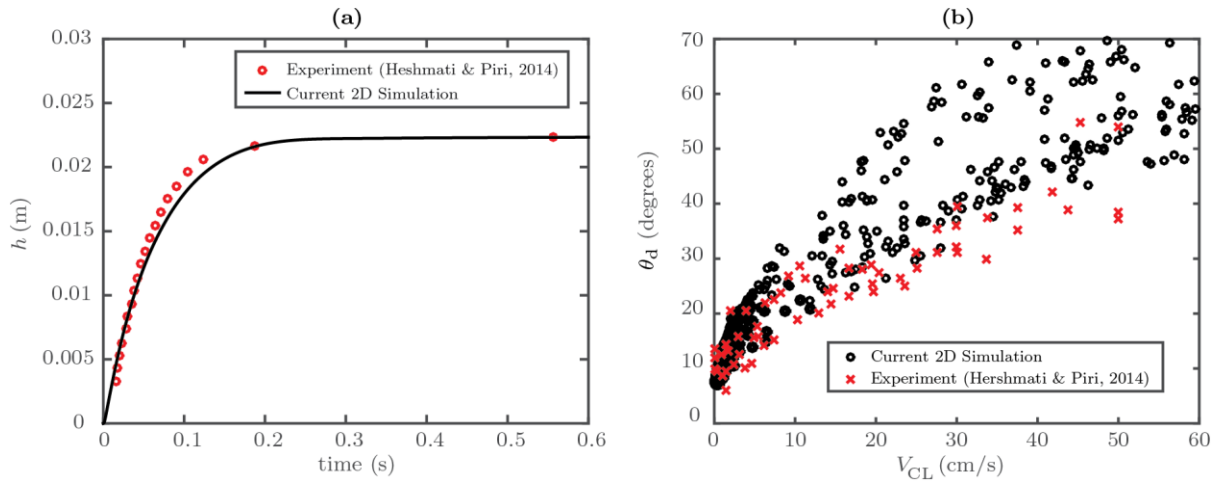

Figure 5-4. Comparisons with experiments of Heshmati & Piri, 2014 for an air-water system: (a) Two-dimensional solution of capillary rise height h vs. time (b) dynamic contact angle $\boldsymbol{\theta_d}$ vs. contact line velocity $\boldsymbol{V_{CL}}$. The radius of the tube $\boldsymbol{r = 0.65}$ mm.

Figure 5-4(a) shows close matching of the average meniscus height h as a function of time when fitted to experimental data for a two-dimensional capillary rise simulation. In order to account for the 2x reduction in curvature due to the two-dimensionality of the simulation compared to the three-dimensional experiment in Heshmati & Piri, 2014, the surface tension σ was doubled in this simulation. Here, the slip length β^* was varied to fit the experimental data until close matching of the liquid rise dynamics was achieved for a given grid resolution. Figure 5-4(b) shows a scatter plot of the dynamic contact angle θ_d vs. contact line velocity V_{CL} compared with the experiment. For higher V_{CL}, the contact angle deviates quite sharply from the static contact angle of water owing to the rapid rise of the meniscus. However, as the meniscus reaches the equilibrium height, the contact angle assumes the static angle until $V_{CL} = 0$ and is in a static configuration. Our agreement with the experiments Heshmati & Piri, 2014 is excellent and demonstrates the ability of our model to capture the interdependency of the contact line velocity and the dynamic angle, which is the ultimate goal of any phenomenological wetting model.

Figure 5-5(a) is a three dimensional capillary rise simulation compared with the same experiment presented in Figure 5-4. For circular capillaries, the experimental matching is once again excellent. Also simulated is a square capillary with the edge length equal to twice the tube radius. Necessarily, the meniscus in the square capillary tube settles at a lower equilibrium height due to an overall increase in surface area compared to a circular tube, thus lowering the overall curvature of the meniscus. A demonstration of a variety of three-dimensional interface shapes is shown in Figure 5-5(b-e) for a fixed static angle. For a triangular tube, the meniscus tends to wick into the corners due to the increase in local curvature there. The effect of the corners is diminished as the angle between the corners decreases, until the meniscus of the circular capillary is recovered. This demonstrates our ability to capture accurate three-dimensional menisci in rather complex geometries, which is useful in capturing the complex interfaces that may be present in strongly heterogeneous fractures and pore-networks.

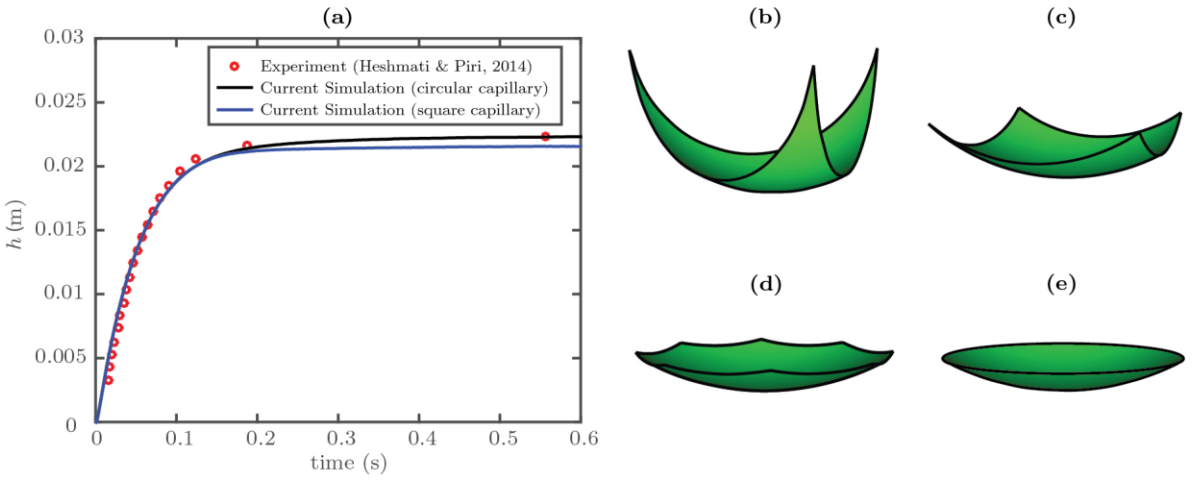

Figure 5-5. (a) Comparison of rise times with experiments Heshmati & Piri, 2014 for circular and square capillaries. Visualizations of interface shapes at $\boldsymbol{\theta_s = 30^\circ}$ for (b) triangular, (c) square, (d) octagonal and (e) circular capillary tubes.

Capturing the correct pressure distribution through pore throats is critical in determining the dynamic and steady-state distributions of immiscible fluids moving through complicated pore networks. For instance, in extremely heterogeneous porous structures (sandstones and shales), displacement of an residual fluid with an invading fluid can lead to complicated flow patterns and saturation profiles that must be accurately captured with a robust modeling of the contact line dynamics. Here, we briefly investigate the flow through a simple pore throat at low capillary numbers for iso-viscous and iso-dense fluids to compare with the value predicted by the Laplace pressure

$$\Delta P = \frac{2\sigma \cos(\theta_s)}{r_t} \tag{16}$$

where r_t is the radius of the throat and is the narrowest portion of the geometry.

The results of a forced flow through a pore-throat is provided in figure 5-6(c). Here, the flow is forced at the bottom boundary at a fixed capillary number and the maximum (or minimum) pressure difference across the inflow and outflow domain $\Delta P = P_{top} - P_{bot}$ is measured. This is plotted as a function of the static contact angle $\theta_s$and fits the expected Laplace pressure described in equation 16 quite favorably for both capillary numbers tested. It is expected that as the capillary number increases, the Laplace pressure will become less important owing to the decreasing influence of surface tension on the flow dynamics.

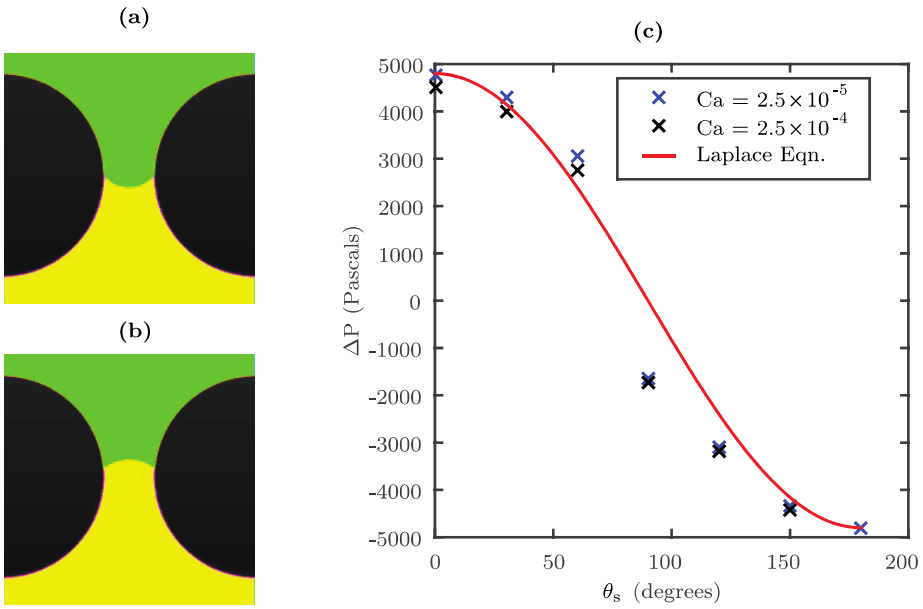

Figure 5-6. Snapshots of flow through a pore throat for (a) $\boldsymbol{\theta_s = 30^\circ}$, (b) $\boldsymbol{\theta_s = 120^\circ}$. Yellow and green contours indicate invading and residual fluid, respectively. The black region represents a solid wall boundary; (c) Comparison of the numerical simulation with the Laplace equation (equation 16).

A snapshot of two simulations at $\theta_s = 30^\circ$ and $\theta_s = 120^\circ$ as the flow passes through the pore throat is shown in figures 5-6(a) and 5-6(b), respectively. Here, the yellow contour represents the invading fluid, and the green contour represents the residual fluid. The flow direction is from bottom to top. For $\theta_s = 30^\circ$ (figure 5-6(a)), the interface curvature indicates that the flow will tend to wick into the pore (owing to the wetting line force having a component in the upward direction) giving a positive value of ΔP for a fixed inflow mass flux. For $\theta_s = 120^\circ$ (figure 5-6(b)) the curvature is inverted compared to the previous case and ΔP is expectedly negative. These results demonstrate the applicability of our wetting model to adequately capture the contact line dynamics occurring at low capillary numbers through pore-throats for use in multiphase flow simulations in heterogeneous porous geometries.

6. TWO-PHASE WETTING IN A REAL FRACTURE

6.1. Using CDFEM to generate meshes

Here, we will briefly describe the procedure in which CDFEM is used to discretize a micro-CT scan of a real fracture into a suitable unstructured, tetrahedral mesh in Aria. First, micro-CT data is post-processed into a matrix of voxels, which describe the geometry as a series of triangles. The voxels are put into a StereoLithography (STL) format which is then read into Aria. CDFEM is used to discretize the interface on the background mesh provided in the input deck. This new conformal mesh is then output in the Exodus file format. This mesh can then be used in a multiphase flow simulation within the fracture geometry.

6.2. Static meniscus in a vertical fracture

6.2.1. Experimental observation

The assembled fracture network (Figure 4-2) was used to measure the meniscus of water displacing the air in a vertical direction. As shown in Figure 6-1, a static water table was set inside the fracture network with the microCT system. MicroCT color image in Figure 6-1a represents continuous scanning result from the front, so the water table looks flat rather than undulating as in the slice of microCT image (Figure 6-1(b)). MicroCT has been used to scan the fracture network before and after water injection. Static conditions were established at three different locations.

Here we report the case with the water table located in the middle of the fracture network. To compute the contact angle, a stack of 3D images was segmented as shown in Figure 6-1(c&d). Over a small region including the meniscus in each image, the fracture region was masked with microCT image of the empty (i.e., no water) fracture network (e.g., white area in Figure 6-1(c)). For this purpose, we used the upper contrast of water-air interface to identify the threshold of each image using the Otsu method (Otsu, 1979). Since it is not practical to compute the contact angle of each meniscus manually (e.g., 540 images), the automatic contact angle algorithm developed in Klise et al. (2016) was used to compute contact angle over the entire collection of 3D segmented images. In this algorithm, the first step is to define the interface between air and water and between solid (i.e., matrix) and water, along with contact points where the solid, water, and air intersect. After each contact point and all interfaces are identified, a plane is fit to the each interface within search volume. Due to segmentation artifact and low resolution of image, it is not typical to obtain the contact angle at all contact points. Here we analyzed 250 contact angles out of possible 1080 contact points (two per each image). The distribution of contact angle is shown in Figure 6-1(e). The contact angle calculation can be improved with high resolution images through interpolation. As mentioned earlier, the aperture in the assembled fracture was higher than actual fracture network. However, the contact angle distribution would be similar since the wettability and other factors to contribute to the contact angle are not significantly influenced by the extra spacing due to the gasket.

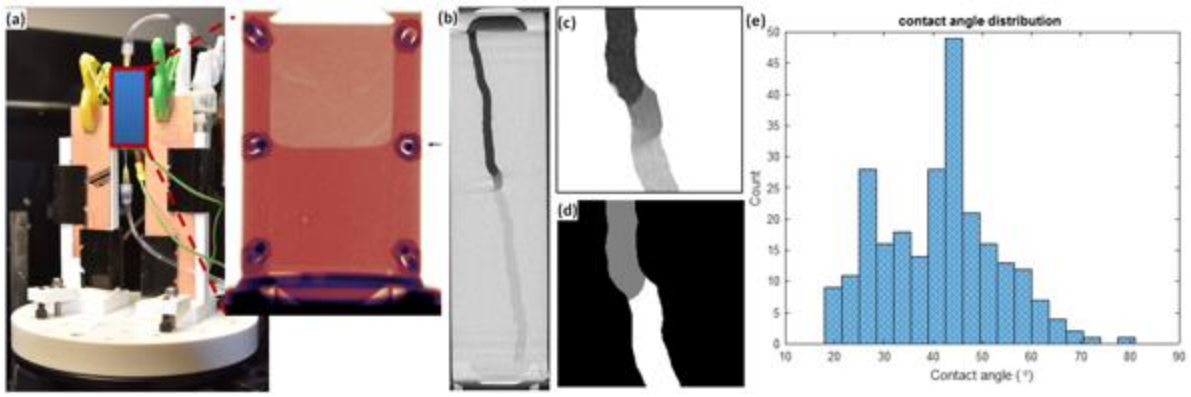

Figure 6-1. (a) MicroCT setup with the assembled fracture network. MicroCT color image is continuously scanned image over time to evaluate the static water table. (b) MicroCT image with dark region for air and light grey for water. (c) ROI for the water meniscus. (d) Segmented image showing the water-air interface. (e) Contact angle distribution of the meniscus over the 3D image stack (mean=41.5°, std=11.95°, minimum=19.0°, and maximum=80.5°).

6.2.2. Numerical simulations

In this section, the static configuration of a two-phase meniscus is obtained in the real fracture geometry using the aforementioned CDFEM framework and wetting model described in Section 5. The fracture geometry was obtained using micro-CT scanning technology in which the heterogeneous roughness and aperture fields were captured in high-fidelity. The shapes of the meniscus are shown in Figures 6-2, 6-3, and 6-4 for various wetting configurations ($\theta_s = 120°, 100°, 55°$), respectively.

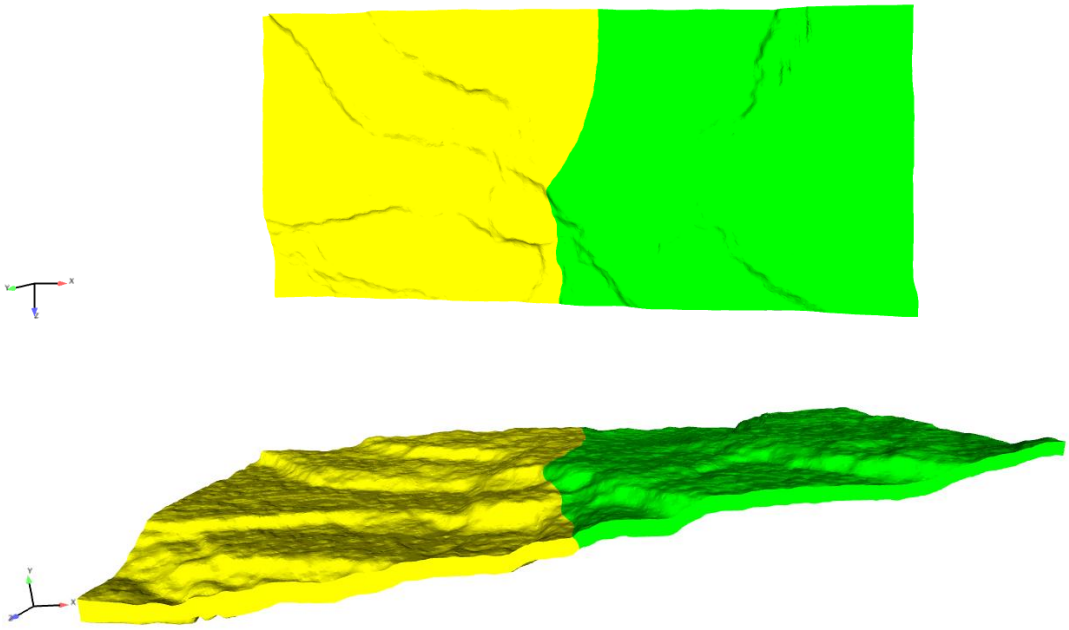

Figure 6-2. Static shape of the two-phase meniscus for a non-wetting (yellow) fluid $\boldsymbol{\theta_s = 120°}$. Top view (top) and isometric view (bottom), fracture openings are on the y-z planes.

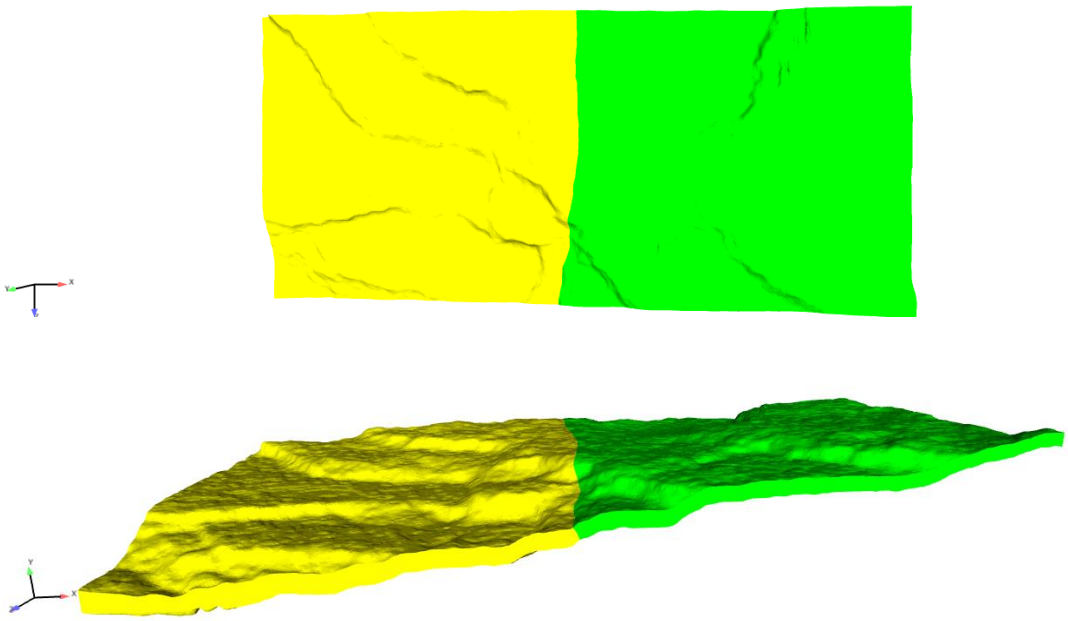

Figure 6-3. Static shape of the two-phase meniscus for a weakly non-wetting (yellow) fluid $\boldsymbol{\theta_s = 100}$°. Top view (top) and isometric view (bottom), fracture openings are on the y-z planes.

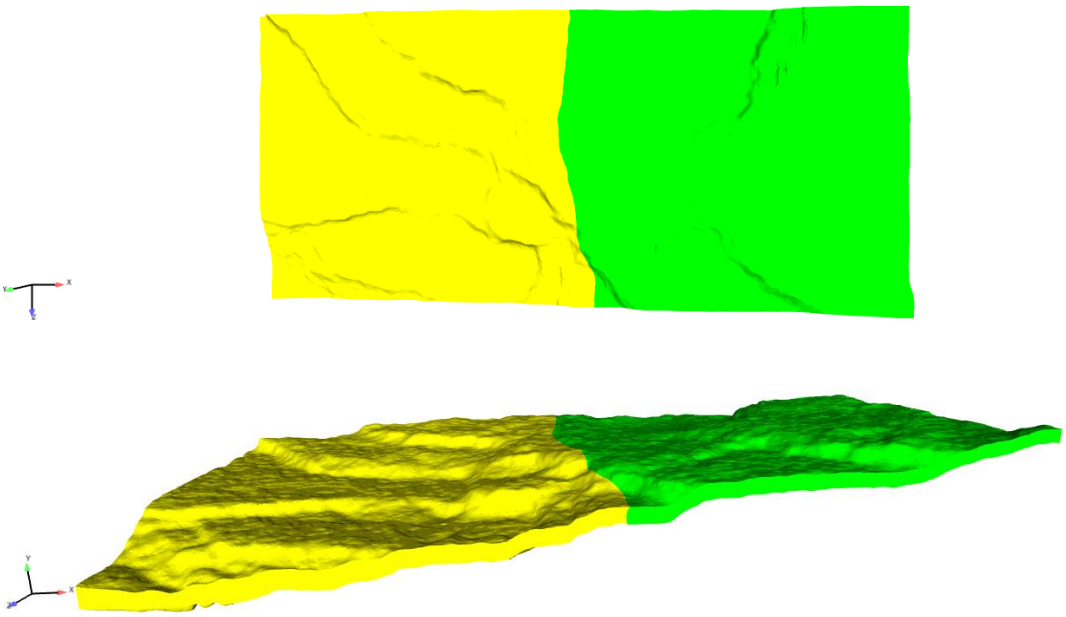

Figure 6-4. Static shape of the two-phase meniscus for a wetting (yellow) fluid $\boldsymbol{\theta_s = 55}$°. Top view (top) and isometric view (bottom), fracture openings are on the y-z planes.

Spanwise (z) variation of the meniscus shapes in all three cases is observed, and can be attributed to the heterogeneity of the fracture aperture in that direction. In cases where the fluid is non-wetting (Figure 6-2), the meniscus will tend to recede in sections of smaller aperture due to large negative capillary pressure. Conversely, in larger aperture sections the meniscus will invade owing to the lower negative capillary pressures. For weakly non-wetting fluid (figure 6-3), the shape of the meniscus is similar to the non-wetting case in figure 6-2, although the spanwise variation is less pronounced. It is expected that for a neutral wetting case ($\theta_s = 90°$), no variation in the meniscus will be observed. In the wetting case (Figure 6-4), the meniscus is again varied in the spanwise direction, but opposes the results for a non-wetting case as described in figure 6-2, owing to the capillary forces are now applied in the opposite direction. That is, in areas where the aperture of the fracture is small, the fluid will tend to imbibe more strongly than in areas of larger relative fracture aperture. As mentioned earlier, the aperture in the 3D printed and assembled fracture was higher than the actual fracture network, so direct comparison of meniscus curvature is not possible. However, the contact angle distribution would be similar since the wettability and other factors to contribute to the contact angle are not significantly influenced by the extra spacing due to the gasket.

7. CONCLUDING REMARKS

This project proposed a novel integration of 3D printing, testing and modeling to develop predictive capability of porous material performance with inherent multiscale physics, aligning it with "resiliency of complex systems." The integration of digital rock physics coupled with 3D printing enables the possibility to print replicas of porous structures for side-by-side testing and physics modeling. The potential impact of such technology is to enable the creation of reproducible custom/functional porous specimens to test material response independent of pore structure variability – a potentially disruptive technology for geosciences. Moreover, it would enable the design of functional porous media with embedded sensors for energy and security applications.

During this 2-year project our technical accomplishments can be listed as:

- Established a workflow for 3D printing models of geologic media, esp. fracture networks and gypsum with rock-like mechanical properties for geomechanics testing
- Developed new Geoscience Imaging & Additive Manufacturing Laboratory (dept. 8864)
- Developed a dynamic wetting model and capability to apply with micro-CT images.
- Analyzed permeability, dispersion characteristics of prototype fractures
- Analyzed and compared experimental (3D printed) and model of two-phase wetting in fractures

A key outcome was establishing a workflow for 3D printing of replicas of geologic media suitable for multiphase flow and geomechanics laboratory testing coupled with multiphysics modeling on the same geometry (digital rock physics). These integrated approaches using 3D printing and numerical simulations of fractured porous media establishes a science-based, rather than empirical, workflow for understanding and predicting fluid-rock interactions in fractured media. This general understanding impacts subsurface resource extraction, waste storage, and energy storage for renewables.

This novel approach positions SNL in a leadership role for the application of 3D printing coupled with digital rock physics in DOE Basic Energy Science R&D programs and other geoscience-related programs in DOE offices (e.g., Fossil Energy, Renewable Energy, Nuclear Energy). It also positions SNL for developing strategic partnership projects with oil and gas industry and/or international collaborators.

REFERENCES

Bobby, S.S., 2014. A preliminary investigation of gypsum bonded moulds by three dimensional printing. *Int. J. Res. Eng. Technol*, 3(06), pp.501-507.

Brown, S.R., 1987. Fluid flow through rock joints: The effect of surface roughness, *Journal of Geophysical Research*, 92(B2), 1337-1347.

Cox, R. G., 1986. The dynamics of the spreading of liquids on a solid surface. part 1. viscous flow, **Journal of Fluid Mechanics**, 168, 169–194.

Dagan, G., 1989, **Flow and Transport in Porous Formations**, Springer-Verlag, Berlin.

Detwiler, R.L., Rajaram, H., and Glass, R.J., 2000. Solute transport in variable-aperture fractures: An investigation of the relative importance of Taylor dispersion and macrodispersion, *Water Resources Research*, 36 (7), 1611-1625.

Dewers, T., Newell, P., Broome, S., Heath, J. and Bauer, S., 2014. Geomechanical behavior of Cambrian Mount Simon Sandstone reservoir lithofacies, Iowa Shelf, USA. International *Journal of Greenhouse Gas Control*, 21, pp.33-48.

Dussan, E.B., 1976. Moving contact line slip boundary condition, *Journal of Fluid Mechanics*, 77, 665-684.

Fereshtenejad, S. and Song, J.J., 2016. Fundamental study on applicability of powder-based 3D printer for physical modeling in rock mechanics, *Rock Mechanics and Rock Engineering*, 49(6), pp.2065-2074.

Ganesan, S., Rajasekaran, S., and Tobiska, L., 2014. Numerical modeling of the non-isothermal liquid droplet impact on a hot solid substrate, *International Journal of Heat and Mass Transfer*, 78, pp. 670 – 687.

Gibson, I., Rosen, D. and Stucker, B., 2015. **Additive manufacturing technologies: 3D printing, rapid prototyping, and direct digital manufacturing.** 2nd Edition. Springer, New York, USA.

Grisak, G.E., and Pickens, J.F., 1980. Solute transport through fractured media 1: The effect of matrix diffusion, *Water Resources Research*, 16 (4), 719-730.

Guo N, Leu MC, (2013) Additive manufacturing: technology, applications and research needs, *Frontiers of Mechanical Engineering*, 8(3), 215–243.

Hoffman, R. L., 1975. A study of the advancing interface. I. interface shape in liquid/gas systems, *Journal of colloid and interface science*, 50(2), pp. 228–241.

Heshmati, M., and Piri, M., 2014. Experimental investigation of dynamic contact angle and capillary rise in tubes with circular and noncircular cross sections, *Langmuir*, 30(47), pp. 14151–14162.

Ingraham, M.D., Bauer, S.J., Quintana, E.C., Bolintineau, D., Rao, R.R. and Lechman, J.B., 2015. Proppant and host rock deformation in fractured shale flow through experiments. *ARMA 15-0102*. In 49th US Rock Mechanics/Geomechanics Symposium. American Rock Mechanics Association.

Jiang, C., Zhao, G.F., Zhu, J., Zhao, Y.X. and Shen, L., 2016. Investigation of dynamic crack coalescence using a gypsum-like 3D printing material. *Rock mechanics and rock engineering*, 49(10), pp.3983-3998.

Ju, Y., Wang, L., Xie, H., Ma, G., Zheng, Z. and Mao, L., 2017. Visualization and transparentization of the structure and stress field of aggregated geomaterials through 3D printing and photoelastic techniques, *Rock Mechanics and Rock Engineering*, 50(6), pp.1383-1407.

Keller, A.A., Roberts, P.V., and Blunt, M.J., 1999. Effect of fracture aperture variations on the dispersion of contaminants, *Water Resources Research*, 35 (1), 55-63.

Klise, K.A., Moriarty, D., Yoon, H. and Karpyn, Z., 2016. Automated contact angle estimation for three-dimensional X-ray microtomography data, *Advances in Water Resources*, 95, pp.152-160.

Noble, D.R., Kucala, A., and Martinez M.J., 2017, A conformal decomposition finite element method for dynamic wetting applications, *Proc. ASME 2017 FED* meeting, July 30 – August 3, Waikoloa.

OpenFOAM, 2017. Open source Field Operation And Manipulation Available at www.openfoam.org .

Otsu, N., 1979. A Threshold Selection Method from Gray-Level Histograms, *IEEE Transactions on Systems, Man, and Cybernetics,* Vol. 9, No. 1, 62-66.

Prosperetti, A., 1981. Motion of two superposed viscous fluids, *The Physics of Fluids*, 24(7), pp. 1217–1223.

Starchenko V., Marra C.J., Ladd A.J.C., 2016. Three-dimensional simulations of fracture dissolution. *Journal of Geophysical Research: Solid Earth*, 121(9):6421–44.

DISTRIBUTION

1	MS0735	Moo Y. Lee	8864 (electronic copy)
1	MS0748	Hector Mendoza	8853 (electronic copy)
1	MS0751	Hongkyu Yoon	8864 (electronic copy)
1	MS0828	Basil Hassan	1510 (electronic copy)
1	MS0828	Sophia Lefantzi	1516 (electronic copy)
1	MS0828	Alec Kucala	1516 (electronic copy)
1	MS0836	David Noble	1516 (electronic copy)
1	MS0885	Mark F. Smith	1801 (electronic copy)
1	MS0899	Technical Library	9536 (electronic copy)
1	MS0359	D. Chavez, LDRD Office	1171 (electronic copy)


Sandia National Laboratories